Effects of vessel tortuosity on coronary hemodynamics: an idealized and patient-specific computational study

Natalya Vorobtsova[1], Claudio Chiastra[2,3], Mark A. Stremler[4], David C. Sane[5], Francesco Migliavacca[2], Pavlos Vlachos[6*]

[1] Department of Mechanical Engineering, Virginia Tech, Blacksburg, Virginia, USA

[2] Laboratory of Biological Structure Mechanics (LaBS), Department of Chemistry, Materials and Chemical Engineering "Giulio Natta", Politecnico di Milano, Milan, Italy

[3] Department of Biomedical Engineering, Thoraxcenter, Erasmus University Medical Center, Rotterdam, The Netherlands

[4] Department of Biomedical Engineering and Mechanics, Virginia Tech, Blacksburg, Virginia, USA

[5] Section of Cardiology, Carilion Clinic, Virginia Tech Carilion School of Medicine, Roanoke, Virginia, USA

[6] School of Mechanical Engineering, Purdue University, West Lafayette, Indiana, USA

* Corresponding Author

Address for correspondence:

Pavlos Vlachos

School of Mechanical Engineering

Purdue University

585 Purdue Mall

West Lafayette, IN

United States

E-mail: pvlachos@purdue.edu

1 Abstract

2 Although coronary tortuosity can influence the hemodynamics of coronary arteries, the
3 relationship between tortuosity and flow has not been thoroughly investigated partly due
4 to the absence of a widely accepted definition of tortuosity and the lack of patient-
5 specific studies that analyze complete coronary trees. Using a computational approach
6 we investigated the effects of tortuosity on coronary flow parameters including pressure
7 drop, wall shear stress, and helical flow strength as measured by helicity intensity. Our
8 analysis considered idealized and patient-specific geometries. Overall results indicate
9 that perfusion pressure decreases with increased tortuosity, but the patient-specific
10 results show that more tortuous vessels have higher physiological wall shear stress
11 values. Differences between the idealized and patient-specific results reveal that an
12 accurate representation of coronary tortuosity must account for all relevant geometric
13 aspects, including curvature imposed by the heart shape. The patient-specific results
14 exhibit a strong correlation between tortuosity and helicity intensity, and the
15 corresponding helical flow contributes directly to the observed increase in wall shear
16 stress. Therefore, helicity intensity may prove helpful in developing a universal
17 parameter to describe tortuosity and assess its impact on patient health. Our data
18 suggest that increased tortuosity could have a deleterious impact via a reduction in
19 coronary perfusion pressure, but the attendant increase in wall shear stress could afford
20 protection against atherosclerosis.

21 **Key words:** Coronary artery; tortuosity; computational fluid dynamics; wall shear stress;
22 helicity.
23

1 Introduction

Coronary vessel tortuosity is an anatomical variant in which the epicardial vessels display abnormally curved or helically coiled paths (1-5). Cardiologists often encounter coronary tortuosity, but its mechanisms and impacts are not well studied or understood. Although coronary tortuosity has been associated with coronary artery disease (1), it can also occur in the absence of significant stenosis (2). Tortuosity has been commonly associated with hypertension (6, 7) and aging (2-4, 6, 8) and has been observed in long standing collateral vessels that form after myocardial infarction (3). Arterial tortuosity has been observed in a variety of other organ systems (9-11), where age-dependent degeneration of elastin fibers is considered a potential etiologic factor, (2) and in some cases there appears to be a genetic predisposition (12-14). While mild tortuosity is often asymptomatic, severe tortuosity may lead to angina, positive stress test, or other manifestations of myocardial ischemia (1, 2, 6, 15).

Tortuosity has been characterized using a variety of mathematical parameters. These include: the distance metric or relative length variation (1, 13, 16-20); the inflection count metric (13); the sum of angles metric (13); the total torsion (21); the total curvature (18, 21); the average torsion (16); the average curvature (16); the total squared curvature (18); and the normalized root-mean squared curvature (10, 14). Some of these metrics are appropriate for specific types of tortuosity. For example, the sum of angles is good for measuring the tortuosity of tight low-amplitude coils, while the distance metric and inflection count metric are good for characterizing vessels with broad meandering curves (13).

Vessel curvature and torsion induce secondary flow (22). Curvature generates circumferential flow (23), first investigated by Dean (24), creating helical fluid motion. As a result, the pressure drop in an idealized curved pipe is larger than the pressure drop, for the same flow rate, in a corresponding straight pipe of the same length (25, 26). Torsion breaks the symmetry of the curvature-generated helical motions making one helical structure more dominant (22). The pressure drop required for blood flow through

3

1   an idealized helically coiled vessel grows with the number of helical coils for the same

2   vessel length (27). Patient-specific numerical simulations have shown that the blood

3   flow resistance increases in the presence of tortuosity in coronary arteries (28).

4   Atherosclerotic lesions appear in regions of low or oscillatory wall shear stress (WSS),

5   or regions of "disturbed" WSS (29). The influence of tortuosity on the susceptibility of

6   arteries to atherosclerosis is not understood, in part because coronary tortuosity, or

7   tortuosity in general, is not well defined in the literature and only a limited number of

8   patient-specific studies have been performed. Moreover, contradiction exists regarding

9   the development of atherosclerosis in tortuous coronary arteries. A clinical study by Li *et*

10   *al.* showed that coronary tortuosity could have a suppressing effect on atherosclerosis

11   (30). In contrast, a numerical study by Xie *et al.* suggested that severe coronary

12   tortuosity could lead to atherosclerosis (28, 31). Theoretical, experimental, and

13   numerical investigations of different aspects of tortuosity such as flow in bends of

14   constant curvature (24, 25, 32, 33), helically coiled pipes of constant curvature and

15   torsion (25, 27), idealized helical arterio-venous graft designs (34), S-shaped pipes with

16   planar centerline (22, 31, 35) and with torsion (22, 36), and two subsequent S-shaped

17   vessels (22), have shown different impacts on WSS. For example, a numerical

18   investigation of flow in a curved pipe without torsion showed extensive regions of

19   disturbed WSS (31). Torsion, on the other hand, leads to more complex flow patterns,

20   reducing the areas exposed to atherogenous conditions (34), leading to more uniform

21   spatial distribution of WSS (23), which reduces the risk of vessel occlusion (37). Clinical

22   and numerical studies of femoral arteries have shown that tortuosity may cause

23   atherosclerosis (17, 19), while the numerical study by Gallo *et al.* showed tortuosity of

24   the carotid bifurcation to be atheroprotective (16).

25   This work explored the dependence of flow parameters on vessel tortuosity and

26   investigated the correlation between tortuosity, pressure drop, and WSS distribution for

27   idealized and patient-based geometries. In the analysis of the idealized cases we

28   focused on the influence of torsionless curvature on the flow in the vessel. In contrast to

29   previous studies (22, 31, 35), each idealized vessel consists of segments with

30   progressively increasing curvature and the vessel diameter tapers uniformly along the

4

1 vessel length, thus providing better physiological fidelity. The geometric parameters,

2 such as the number of coils, the amplitude of coils, and the tapering angle, were

3 obtained from clinical data. Coronary trees from three subjects are investigated for the

4 patient-specific cases. Each vessel of the coronary trees was individually analyzed,

5 resulting in 23 segments, thus allowing for statistical analysis of the effect of coronary

6 tortuosity on hemodynamic parameters. Finally, we explored if intensity of the helical

7 flow can capture the effects of tortuosity and thus serve as a parameter to describe flow

8 alterations and potential health risks.

2 Materials and methods

2.1 Models of arterial geometries

2.1.1 Idealized geometries

12 Idealized 3D geometries of tortuous coronary vessels were modeled in order to

13 compare flow parameters in vessels with different numbers of curved arcs but without

14 torsion or branching. The centerline of each vessel was taken to lie on a plane. Three

15 cases were considered, denoted T-5, T-6, and T-7 (Figure 1 a–c), where the integer

16 signifies the number of curved arcs in the vessel. The amplitude of each subsequent

17 bend is smaller than that of the previous bend. All cases have an inlet radius of 1.5 mm

18 and taper uniformly to a final radius of 0.75 mm.

2.1.2 Patient-specific geometries

20 Computed Tomography Angiograms (CTA) from three patients (patient-A, -B, and -C)

21 were used to generate 3D geometries. The use of these data was approved by the

22 ethical committee of Carilion Clinic (Roanoke, VA, USA) and informed consent was

23 obtained for this study. The left coronary artery tree was segmented from each CTA

24 using ITK-SNAP (38). Each segmentation was manually improved in locations where

25 the automatic segmentation failed, smoothed, and exported to CAD using MeshLab (39)

26 and Geomagic Studio® (3D Systems, Cary, NC, USA). The resulting geometries for all

27 three cases are shown in Figure 1 (d-f).

5

2.1.3 Post-processing and centerline extraction

For post-processing of the idealized cases, the straight sections at the beginning and end of each vessel were excluded from the analysis, as shown in Figure 2a. The horizontal distance from the vessel inlet to points P1 and P2 is the same for all cases. For post-processing of the patient-specific cases, bifurcating regions were excluded, and each vessel tree was split into individual segments, as shown in Figure 2b. Splitting the three patient-specific cases gives 23 vessel segments, which, in contrast to the idealized cases, allowed for a statistical analysis of the solution.

For each vessel segment we determined its geometric centerline (21, 40, 41), which can be described parametrically by means of a curvilinear variable s as

$$g(s) = \big(x(s), y(s), z(s)\big) . \tag{1}$$

A local fifth-order polynomial filter with Gaussian kernel is used to reduce high-frequency noise from patient-specific data obtained during segmentation and centerline tracking (20, 42). Deviation of the centerline from a straight line at each point is given by the curvature

$$k(s) = \frac{\left| g'(s) \times g''(s) \right|}{\left| g'(s) \right|^3} , \tag{2}$$

where the prime denotes differentiation with respect to s. Torsion, a measure of how sharply the curve is twisting out of the plane of curvature, is calculated as

$$t(s) = \frac{\big(g'(s) \times g''(s)\big) \times g'''(s)}{\left| g'(s) \times g''(s) \right|} . \tag{3}$$

2.1.4 Tortuosity metrics

Three standard metrics were used to characterize the degree of tortuosity. The distance metric,

6

1
$$DM = \frac{L}{l} \, , \tag{4}$$

2 quantifies the "lengthening effect" of tortuosity (1, 13), where L is the total path-length of
3 the centerline and *l* is the straight-line distance between the beginning and end of the
4 segment. The total curvature,

5
$$TC = \int_0^L \kappa(s)\,ds \, , \tag{5}$$

6 and total torsion ,

7
$$TT = \int_0^L |\tau(s)|\,ds \, , \tag{6}$$

8 are calculated by integrating the curvature and the absolute value of torsion,
9 respectively, along the centerline (17, 18, 21, 41).

2.2   Computational fluid dynamics modeling
2.2.1   Boundary conditions and simulation settings

12 Pulsatile flow simulations were performed using ANSYS Fluent 14.5 (ANSYS Inc.,
13 Canonsburg, PA, USA). For both the idealized and patient-specific cases, a uniform
14 velocity profile designed to match coronary artery flow waveforms (44) was imposed at
15 the inlet. Following van der Giessen e*t al.* (45), the average flow rate for each patient-
16 specific case was adjusted according to

17
$$q = 1.43 d^{2.55} \, , \tag{7}$$

18 where q is the flow rate and d is the inlet diameter. The outlet boundary condition for
19 the idealized cases was taken to be a constant reference pressure. For the patient-
20 specific cases, the outlet boundary condition was taken to be a time-dependent
21 pressure based on a lumped parameter resistance model, with the outlet pressure

7

1   calculated at each time step as

2    $$p(t) = R{\times}q(t) \ , \tag{8}$$

3   where R is the resistance of the downstream vascular system. Resistance values were
4   adopted from Pietrabissa *et al.* (46). No-slip boundary conditions were imposed on the
5   vessel walls, which were assumed rigid. The blood density was assumed to be
6   constant, $\rho=1060$ *kg m^{-3}*, and the Carreau model (47) was used to model the blood as a
7   non-Newtonian fluid. Flow was assumed to be laminar.

8   A coupled solver was used with a second-order upwind scheme. The convergence
9   criterion for continuity and velocity residuals was set to give a relative error less than
10   0.01%.Coupled grid and time sensitivity analysis is performed. For idealized and
11   patient-specific cases, 100 and 800 time steps were used per cardiac cycle,
12   respectively. Three cardiac cycles were simulated to ensure temporal periodicity of the
13   solution.

14   Grid and time sensitivity analyses were performed to ensure independence of the
15   results on the mesh and time step size. For patient-specific study, coarse, medium, and
16   fine were considered with 1487340, 702440 and 3045176 elements, respectively. Time
17   step for each mesh was set to 0.002115 s, 0.001551 s, 0.00116325 s respectively,
18   which corresponded to 440, 600, and 800 time steps per cardiac cycle. Thus, the time
19   step was refined equally to the mesh size refinement. The sensitivity analysis showed
20   that the relative discretization error for the fine mesh does not exceed 0.1% for selected
21   pressure and wall shear dependent flow parameters.

22   **2.3   Quantification of results**

23   The pressure drop along the tortuous vessel segment was quantified by calculating the
24   time-averaged difference between the area-weighted average of the pressure values at
25   the entrance and exit of the vessel segment per unit length, $\frac{\mathrm{D}P}{L}$.   For the idealized

26   cases, $\frac{\mathrm{D}P}{L}$ is non-dimensionalized by the value for an equivalent straight vessel of the

8

1 same total length. For patient-specific cases, $\frac{DP}{L}$ is non-dimensionalized by the viscous

2 scale (48). Hereafter, $\frac{DP}{L}$ will refer to the non-dimensionalized pressure drop per unit

3 length.

4 Both experimental (49) and theoretical (24, 50) studies have shown that curvature and

5 torsion contribute to the initiation and development of helical flow patterns. Hence, we

6 calculate the local normalized helicity (LNH), which describes the interplay between

7 rotational and translational motion (16, 34, 51-54):

8
$$LNH = \frac{(\nabla \times v) \cdot v}{|\nabla \times v| \cdot |v|} = \cos \alpha \ , \tag{9}$$

9 where α is the angle between the velocity vector v and the vorticity vector $(\nabla \times v)$.

10 Positive or negative values of *LNH* indicate clockwise or counter-clockwise rotating

11 structures along the flow direction, respectively. We also considered the helicity

12 intensity of the flow,

13
$$h_2 = \frac{1}{TW} \int_0^T \int_W |(\nabla \times v) \cdot v| dW dt \ , \tag{10}$$

14 where W is the volume of the segment and *T* is the duration of a cardiac cycle (16, 51).

15 Calculating *LNH* helps visualize flow patterns (16, 34, 51-54), while h_2 captures the

16 strength of the helical flow (16, 51). Previous studies have shown that for carotid

17 bifurcations h_2 is curvature-driven, and high values of h_2 suppress disturbances of the

18 WSS distribution (16, 51). The helicity intensity h_2 can be non-dimensionalized as $\frac{h_2 \times L}{V^2}$,

19 where L is the centerline length and V is the volume-averaged and time-averaged

20 velocity of each vessel segment." To study the dependence of h2 on the degree of

21 tortuosity, we calculated the helicity intensity. Correlation between vessel geometry and

22 helical flow was determined through regression analysis of h_2 versus the tortuosity

23 metrics DM, TT, and TC.

24 Another important quantity is the WSS, which we evaluated in terms of the time

9

1 averaged wall shear stress (TAWSS) distribution (55). Areas of the vessel wall with low

2 TAWSS (smaller than 0.5 Pa) correlate with a higher risk for atherosclerosis (56, 57).

3 This correlation is attributed to increased uptake of blood-borne particles in areas of low

4 WSS (58). The risk may increase if the particles stay near the wall for a relatively long

5 time. The residence times of particles near the wall were evaluated using the Relative

6 Residence Time (RRT) defined in (59). Regions of high RRT are regions near the wall

7 where particles move slower than in regions of low RRT. When occurring in combination

8 with low TAWSS, regions of high RRT are associated with an increased risk of coronary

9 artery disease (60). Hereafter, we refer to regions that have both low TAWSS and high

10 RRT as regions of "disturbed WSS". Following Lee *et al.* (61, 62), we characterize the

11 TAWSS and RRT distributions for each segment by two threshold values for which 90%

12 of the vessel segment surface is exposed to higher TAWSS and lower RRT than

13 corresponding TAWSS and RRT thresholds. Those thresholds are denoted as

14 TAWSS90 and RRT90.

3 Results

3.1 Idealized study

17 We investigated simple geometries in order to explore basic dependencies between the

18 parameters of interest. Table 1 presents the calculated tortuosity metrics and geometric

19 descriptors, such as average radius, average tapering, and vessel length, for the three

20 idealized cases T-5, T-6, and T-7. As expected, DM (equation 4) and TC (equation 5)

21 grow with the number of curved arcs.

22 Dimensionless pressure drop for the tortuous part of the main vessel increases with the

23 number of curved segments, as shown in Figure 3a, as well as with the tortuosity

24 degree of the main vessel. Figure 3b also shows that the helicity intensity is higher for

25 those cases with a larger number of curved segments. In addition, these results indicate

26 that a more tortuous vessel has a lower TAWSS90 and higher RRT90 (Figure 3 c-d),

27 resulting in larger area of lower TAWSS and a larger area of higher RRT. It is evident

28 that helicity intensity changes significantly with the number of arcs, while the

29 hemodynamic parameters increase by about 5%. Hence, there is a relationship

10

1   between the number of curved arcs and the flow parameters.

2   ## 3.2   Patient-specific study

3   ### 3.2.1   Relation between tortuosity metrics

4   We analyzed 23 segments of 3 patient-specific coronary trees to investigate the

5   influence of realistic geometry on arterial flow. The corresponding tortuosity metrics and

6   geometric descriptors for each vessel segment are presented in Table 2. Figure 4a

7   shows the variation of total torsion with the corresponding total curvature. These results

8   reveal the varying severity of non-planarity and curvature in the left coronary arteries. It

9   is worth noting that the minimum total torsion for any of the 23 vessel segments was

10   found to be approximately 4.7, indicating that all of the vessels exhibit substantial

11   torsion. There is also a weak positive correlation between the total torsion and total

12   curvature for these vessels, as shown by the linear regression of $R^2 = 0.45$. Figure 4 (b)

13   and (c) show a positive correlation between DM and TT and TC with $R^2=0.42$ and

14   $R^2=0.56$, respectively, suggesting that the lengthening of a vessel affects the curvature

15   and torsion of the vessel and vice versa.

16   ### 3.2.2   Flow Patterns

17   Representative flow patterns from each of the three patient-specific cases are shown in

18   Figures 5, 6, and 7. The corresponding cases are indicated by red circles in Figure 4.

19   Two of the three vessels (patient-A, patient-C) do not have a pronounced helically

20   coiled shape, and torsion is mainly due to the curvature of the heart. In contrast, the

21   vessel for patient-B has torsion due to a significantly helically coiled shape. For the

22   vessel segment of patient-A (Figure 5a), we selected three cross-sections (Figure 5c)

23   and determined the axial velocity magnitude at each of them, as shown in Figure 5 (d-f).

24   The WSS distribution is shown in Figure 5g. LNH iso-surfaces (LNH=±0.4), shown from

25   two angles in in Figure 5h, highlight the presence and shape of helical structures in the

26   branch flow. The corresponding plots for patient-B and patient-C are shown in Figure 6

27   and 7.

28   We observed helical counter-rotating structures in multiple regions of the vessel tree,

11

1   which can be attributed to the high values of the Dean number ($K = \dfrac{\rho V d}{\mu}\left(\dfrac{d}{R}\right)^{1/2}$, where d

2   is the local diameter, R is local curvature radius, V is an average velocity on the cross-

3   section, μ is the dynamic viscosity of the flow, and ρ is density of the blood) (24, 63). It

4   has been shown that secondary flow is dependent on this parameter (33, 49). For very

5   small values of K, the flow can be approximated as Poiseuille flow, and increasing K

6   gives rise to secondary flow. The maximum K is 123.98 for patient-A, 148.33 for patient-

7   B, and 352.36 for patient-C; for all of these we expect two vortical structures to appear

8   (33).

9   Figure 5 (d-f) for patient-A, Figure 6 (d-f) for patient-B, and Figure 7 (d-f) for patient-C

10   show that the velocity profiles are skewed towards the outer side of the distal part of the

11   bend. Regions of local maximum WSS are also located on the outer side of the distal

12   part of the bend (Figure 5g, Figure 6g, Figure 7g). The position and intensity of the peak

13   velocity and WSS distribution are dependent on the vessel geometry. All three vessels

14   show helical structures in the curved parts of the vessel, as depicted in Figure 5h,

15   Figure 6h and Figure 7h. For patient-A and patient-C, these structures are relatively

16   symmetric, while for patient-B a clock-wise rotating structure dominates.

17   Similar to Gallo *et al.* (16, 51), we investigated how the strength of the helical flow

18   depends on tortuosity and if the flow parameters of interest are affected by it. Figure 8

19   shows a statistically significant dependence of the helicity intensity (h^2) on TC (R^2 =

20   0.7); slightly weaker correlations are observed for DM (R^2 = 0.55) and TT (R^2 = 0.58). In

21   all cases, the helicity intensity is positively correlated with tortuosity metrics, indicating

22   that a larger tortuosity causes higher intensity of the helical flow.

23   To elucidate how the pressure drop and WSS change when the flow in the vessel

24   becomes more helical due to the tortuosity, we investigated a correlation between the

25   flow parameters of interest and the helicity of the flow for each vessel. Figure 9 shows

26   pressure drop per unit length, TAWSS90, and RRT90 vary with the helicity intensity for

27   all of the segments. The plots show clear positive correlation of the dimensionless

28   pressure drop per unit length and dimensionless helicity intensity with R^2 = 0.67 (Figure

12

1 9a), positive correlation of TAWSS90 and h_2 with R^2 = 0.62 (Figure 9b), and negative

2 correlation of RRT90 and h_2 with R^2 = 0.73 (Figure 9c). In agreement with the results of

3 the idealized cases, there is a pronounced increase in the pressure drop per unit length

4 of the vessel as the helicity intensity of the flow increases in more tortuous vessels.

5 However, unlike the idealized cases, Figure 9 (b) and (c) show that the higher helicity

6 intensity is a strong predictor that a smaller vessel area will be subjected to low TAWSS

7 and large RRT.

4 Discussion

9 Tortuosity is considered a predictor of abnormal coronary hemodynamics leading to

10 reduced perfusion (2, 15) and, potentially, to an increased risk of atherosclerosis (1, 2,

11 31, 64, 65). The current study investigated how different aspects such as curvature,

12 torsion, and lengthening due to tortuosity affect the pressure drop, WSS, and RRT. We

13 performed calculations of the 3D idealized and patient-based geometries. The idealized

14 geometries represent a simplified tortuous coronary artery without branches and were

15 designed to investigate the curvature aspect of tortuosity in the absence of torsion. The

16 patient-specific models were produced from 3D coronary CTs of the left coronary tree.

17 We found a correlation between total curvature and torsion metrics and that torsion is

18 present for each segment due to the shape of the heart.

19 Our investigation revealed a complex relation between tortuosity metrics and

20 hemodynamic parameters that is governed by helicity intensity. Visualization of the flow

21 indicated that helical motion is very pronounced in tortuous vessels, and calculations for

22 both idealized and patient-based cases showed a pronounced correlation between

23 tortuosity and helicity intensity. We observed that an increasing tortuosity is a

24 statistically significant predictor of enhanced helicity intensity.

25 The relationships between tortuosity metrics, helicity intensity, and pressure drop per

26 unit length indicate that tortuosity can cause decreased perfusion. The dimensionless

27 pressure drop per unit length of the vessel is positively correlated with the non-

28 dimensional helicity intensity. For both the idealized and patient-specific cases, there is

13

1   an increase in pressure drop per unit length with increasing tortuosity.

2   Previously, it has been reported that regions exposed to high RRT and low TAWSS are
3   more susceptible to atherosclerotic lesion formation (29, 56). In this study we used
4   RRT90 and TAWSS90, defined as the higher 10-percentile threshold for RRT and lower
5   10-percentile threshold for TAWSS. Increasing TAWSS90 suggests that the area of low
6   TAWSS is diminishing. Similarly, a decreasing RRT90 signifies a decreasing area of
7   high RRT. By inference (29, 56), reducing RRT90 and TAWSS90 suggests protection
8   against atherosclerosis.

9   The results of the idealized cases show that an increasing degree of tortuosity makes
10   the helicity intensity grow, while values of TAWSS90 and RRT90 decrease and increase
11   respectively. Consequently, this indicates that TAWSS90 and RRT90 are positively and
12   negatively correlated with helicity intensity in the case of zero torsion. However, for the
13   patient-based cases, we observed that the non-dimensional helicity intensity shows an
14   opposite correlation with the WSS derived descriptors. Thus, our results show that,
15   when torsion is present, real tortuous artery vessels are potentially less prone to
16   atherosclerosis. This finding represents an important difference between the idealized
17   and patient specific cases and is attributed to the fact that, in reality, tortuous vessels
18   have significant torsion due to the heart shape. Our results suggest that the torsion
19   present in real tortuous coronary arteries may have a mitigating effect on
20   atherosclerosis.

21   One long-standing challenge with respect to coronary tortuosity is to define one
22   parameter that clearly describes the degree of vessel tortuosity and how flow
23   parameters change with that degree. With such a parameter, it would be straightforward
24   to categorize tortuous vessels and estimate possible cardiovascular implications related
25   to tortuosity. Our study shows that different aspects of tortuosity, like torsion or
26   curvature, have different impacts, and it is not appropriate to use a single tortuosity
27   metric. However, our observations also indicate that helicity intensity strongly depends
28   on the degree of tortuosity and is a statistical predictor of flow alterations that cause
29   pressure drop and WSS change. Thus, even though further investigations are required,

14

1 including the analysis of a possible correlation between helicity indexes and local

2 hemodynamics variables different from TAWSS, and RRT (e.g. wall shear stress

3 gradient), we propose that helicity intensity might be a generalized parameter to

4 describe the effect of tortuosity on coronary flow and its implications on the health of a

5 patient.

6 ## 4.1 Limitations

7 The current study has some limitations. Due to resolution restrictions, the segmentation

8 and smoothing of the patient-based geometries are expected to have introduced errors.

9 For both the idealized and patient-specific models the wall of the vessel was considered

10 rigid. In the patient-specific cases the myocardium was assumed to be non-moving,

11 analyzing only the diastolic geometrical configuration; thus the influence of the

12 displacement of the myocardium during the cardiac cycle is neglected. In addition, only

13 three patient-specific coronary trees were investigated. Despite these limitations, we

14 believe that this study represents an important step toward offering insights into

15 coronary tortuosity and its effect on coronary hemodynamics.

16

15

5   Conclusions

This computational study suggests that tortuosity should be modeled by a parameter that accounts for both curvature and torsion effects of tortuosity. Torsion due to the shape of the heart and torsion due to the acquired helical shape of the vessels should be included. Overall, our study shows that the pressure drop in a coronary artery increases as a function of the tortuosity of the vessel, so the artery might be subject to reduced perfusion. In agreement with previous idealized studies of Xie *et al.* (31, 36), our investigation of idealized cases without torsion shows that tortuosity may *increase* the risk of atherosclerosis. However, our patient-specific analysis shows that tortuosity could *decrease* the risk of atherosclerosis, a result similar to observations of the clinical study of Li *et al.* (30) and a recent investigation of tortuosity of carotid bifurcations (16, 51). This result is a counterintuitive and important finding, signifying that coronary tortuosity in some cases can mitigate the risk of atherosclerosis in patients that may be subject to other atherogenic factors. Finally, our study indicates the significance of helical flow in tortuosity investigations. Future investigations will help determine whether helicity intensity can be used as a generalizable tool to predict and elucidate the consequences of coronary tortuosity on the health of a patient.

6   Acknowledgments

16

1 Conflict of Interest statement

2 Authors Natalya Vorobtsova, Claudio Chiastra, Mark A. Stremler, David C. Sane,
3 Francesco Migliavacca, Pavlos Vlachos have no conflicts of interest to report. No
4 human studies were carried out by the authors for this article. No animal studies were
5 carried out by the authors for this article.

6

17

7   References

1.   Han HC. Twisted Blood Vessels: Symptoms, Etiology and Biomechanical Mechanisms. Journal of Vascular Research. 2012;49(3):185-97.

2.   Zegers ES, Meursing BTJ, Zegers EB, Ophuis AJMO. Coronary tortuosity: a long and winding road. Netherlands Heart Journal. 2007;15(5):191-5.

3.   Hutchins GM, Miner MM, Bulkley BH. Tortuosity as an index of the age and diameter increase of coronary collateral vessels in patients after acute myocardial infarction. The American Journal of Cardiology. 1978;41(2):210-5.

4.   Turgut O, Yilmaz A, Yalta K, Yilmaz B, Ozyol A, Kendirlioglu O, et al. Tortuosity of coronary arteries: an indicator for impaired left ventricular relaxation? Int J Cardiovasc Imaging. 2007;23(6):671-7.

5.   Barilla F, Romeo F, Rosano GMC, Valente A, Reale A. Coronary artery loops and myocardial ischemia. American Heart Journal. 1991;122(1):225-6.

6.   Del Corso L, Moruzzo D, Conte B, Agelli M, Romanelli AM, Pastine F, et al. Tortuosity, kinking, and coiling of the carotid artery: expression of atherosclerosis or aging? Angiology. 1998;49(5):361-71.

7.   Jakob M, Spasojevic D, Krogmann ON, Wiher H, Hug R, Hess OM. Tortuosity of coronary arteries in chronic pressure and volume overload. Cathet Cardiovasc Diagn. 1996;38(1):25-31.

8.   Soikkonen K, Wolf J, Mattila K. Tortuosity of the lingual artery and coronary atherosclerosis. British Journal of Oral & Maxillofacial Surgery. 1995;33(5):309-11.

9.   Cheung CY-L, Zheng Y, Hsu W, Lee ML, Lau QP, Mitchell P, et al. Retinal vascular tortuosity, blood pressure, and cardiovascular risk factors. Ophthalmology. 2011;118(5):812-8.

10.   Dougherty G, Johnson MJ, Wiers MD. Measurement of retinal vascular tortuosity and its application to retinal pathologies. Medical & Biological Engineering & Computing. 2010;48(1):87-95.

11.   Sutter FKP, Helbig H. Familial retinal arteriolar tortuosity: A review. SURVEY OF OPHTHALMOLOGY. 2003;48(3):245-55.

12.   Jackson ZS, Dajnowiec D, Gotlieb AI, Langille BL. Partial off-loading of longitudinal tension induces arterial tortuosity. Arteriosclerosis, thrombosis, and vascular biology. 2005;25(5):957-62.

13.   Bullitt E, Gerig G, Pizer SM, Lin W, Aylward SR. Measuring tortuosity of the intracerebral vasculature from MRA images. IEEE transactions on medical imaging. 2003;22(9):1163-71.

14.   Pletcher BA, Fox JE, Boxer RA, Singh S, Blumenthal D, Cohen T, et al. Four sibs with arterial tortuosity: description and review of the literature. Am J Med Genet. 1996;66(2):121-8.

15.   Gaibazzi N, Rigo F, Reverberi C. Severe Coronary Tortuosity or Myocardial Bridging in Patients

18

With Chest Pain, Normal Coronary Arteries, and Reversible Myocardial Perfusion Defects. The American Journal of Cardiology. 2011;108(7):973-8.

16.   Gallo D, Steinman DA, Morbiducci U. An Insight into the Mechanistic Role of the Common Carotid Artery on the Hemodynamics at the Carotid Bifurcation. Annals of biomedical engineering. 2014.

17.   Wood NB, Zhao SZ, Zambanini A, Jackson M, Gedroyc W, Thom SA, et al. Curvature and tortuosity of the superficial femoral artery: a possible risk factor for peripheral arterial disease. Journal of applied physiology (Bethesda, Md : 1985). 2006;101(5):1412-8.

18.   Hart WE, Goldbaum M, Côté B, Kube P, Nelson MR. Measurement and classification of retinal vascular tortuosity. International journal of medical informatics. 1999;53(2-3):239-52.

19.   Smedby Ö, Bergstrand L. Tortuosity and atherosclerosis in the femoral artery: What is cause and what is effect? Annals of biomedical engineering. 1996;24(4):474-80.

20.   Piccinelli M, Veneziani A, Steinman DA, Remuzzi A, Antiga L. A Framework for Geometric Analysis of Vascular Structures: Application to Cerebral Aneurysms. IEEE Transactions on Medical Imaging. 2009;28; 31(8):1141-55.

21.   O'Flynn PM, O'Sullivan G, Pandit AS. Methods for three-dimensional geometric characterization of the arterial vasculature. Annals of biomedical engineering. 2007;35(8):1368-81.

22.   Alastruey J, Siggers JH, Peiffer V, Doorly DJ, Sherwin SJ. Reducing the data: Analysis of the role of vascular geometry on blood flow patterns in curved vessels. Physics of Fluids. 2012;24(3):031902.

23.   Alastruey J, Khir AW, Matthys KS, Segers P, Sherwin SJ, Verdonck PR, et al. Pulse wave propagation in a model human arterial network: Assessment of 1-D visco-elastic simulations against in vitro measurements. Journal of Biomechanics. 2011;44(12):2250-8.

24.   Dean WR. Note on the motion of fluid in a curved pipe. London, Edinburgh, and Dublin Philosophical Magazine and Journal of Science. 1927;4(20):208-23.

25.   Berger SA, Talbot L, Yao LS. Flow in Curved Pipes. Annual Review of Fluid Mechanics. 1983;15(1):461-512.

26.   Li Y, Shi Z, Cai Y, Feng Y, Ma G, Shen C, et al. Impact of Coronary Tortuosity on Coronary Pressure: Numerical Simulation Study. PLoS ONE. 2012;7(8):e42558.

27.   Kaplan AD, Jaffa AJ, Timor IE, Elad D. Hemodynamic Analysis of Arterial Blood Flow in the Coiled Umbilical Cord. Reproductive Sciences. 2010;17(3):258-68.

28.   Xie X, Wang Y, Zhu H, Zhou H, Zhou J. Impact of Coronary Tortuosity on Coronary Blood Supply: A Patient-Specific Study. PLoS ONE. 2013;8(5):e64564.

29.   Chien S. Effects of disturbed flow on endothelial cells. Annals of biomedical engineering. 2008;36(4):554-62.

19

30.	Li Y, Shen CX, Ji YN, Feng Y, Ma GS, Liu NF. Clinical Implication of Coronary Tortuosity in Patients with Coronary Artery Disease. PLoS ONE. 2011;6(8):e24232.

31.	Xie X, Wang Y, Zhu H, Zhou J. Computation of hemodynamics in tortuous left coronary artery: a morphological parametric study. Journal of Biomechanical Engineering. 2014;136(10):101006.

32.	Pedley TJ. The fluid mechanics of large blood vessels. Cambridge; New York: Cambridge University Press; 1980.

33.	Siggers JH, Waters SL. Steady flows in pipes with finite curvature. Physics of Fluids. 2005;17(7):77102.

34.	Van Canneyt K, Morbiducci U, Eloot S, De Santis G, Segers P, Verdonck P. A computational exploration of helical arterio-venous graft designs. Journal of Biomechanics. 2013;46(2):345-53.

35.	Qiao AK, Guo XL, Wu SG, Zeng YJ, Xu XH. Numerical study of nonlinear pulsatile flow in S-shaped curved arteries. Medical engineering & physics. 2004;26(7):545-52.

36.	Xie X, Wang Y, Zhou H. Impact of coronary tortuosity on the coronary blood flow: a 3D computational study. Journal of biomechanics. 2013;46(11):1833-41.

37.	Caro CG, Cheshire NJ, Watkins N. Preliminary comparative study of small amplitude helical and conventional ePTFE arteriovenous shunts in pigs. Journal of The Royal Society Interface. 2005;2(3):261-6.

38.	Yushkevich PA, Piven J, Hazlett HC, Smith RG, Ho S, Gee JC, et al. User-guided 3D active contour segmentation of anatomical structures: Significantly improved efficiency and reliability. NeuroImage. 2006;31(3):1116-28.

39.	http://meshlab.sourceforge.net/.

40.	Choi G, Cheng CP, Wilson NM, Taylor CA. Methods for quantifying three-dimensional deformation of arteries due to pulsatile and nonpulsatile forces: implications for the design of stents and stent grafts. Annals of biomedical engineering. 2009;37(1):14-33.

41.	Dougherty G, Johnson MJ. Clinical validation of three-dimensional tortuosity metrics based on the minimum curvature of approximating polynomial splines. Medical Engineering and Physics. 2008;30(2):190-8.

42.	Sangalli LM, Secchi P, Vantini S, Veneziani A. A Case Study in Exploratory Functional Data Analysis: Geometrical Features of the Internal Carotid Artery. JOURNAL OF THE AMERICAN STATISTICAL ASSOCIATION. 2009;104(485):37-48.

43.	Sangalli LM, Secchi P, Vantini S, Veneziani A. Efficient estimation of three-dimensional curves and their derivatives by free-knot regression splines, applied to the analysis of inner carotid artery centrelines. Journal of the Royal Statistical Society: Series C (Applied Statistics). 2009;58(3):285-306.

20

44.	Davies JE, Parker KH, Mayet J, Whinnett ZI, Francis DP, Manisty CH, et al. Evidence of a dominant backward-propagating "suction" wave responsible for diastolic coronary filling in humans, attenuated in left ventricular hypertrophy. Circulation. 2006;113(14):1768-78.

45.	van der Giessen AG, Groen HC, Doriot P-A, de Feyter PJ, van der Steen AFW, van de Vosse FN, et al. The influence of boundary conditions on wall shear stress distribution in patients specific coronary trees. Journal of Biomechanics. 2011;44(6):1089-95.

46.	Pietrabissa R, Mantero S, Marotta T, Menicanti L. A lumped parameter model to evaluate the fluid dynamics of different coronary bypasses. Medical engineering & physics. 1996;18(6):477-84.

47.	Seo T, Schachter LG, Barakat AI. Computational study of fluid mechanical disturbance induced by endovascular stents. Annals of biomedical engineering. 2005;33(4):444-56.

48.	Papanastasiou TC, Georgiou GC, Alexandrou AN. Viscous fluid flow. Boca Raton, Fla: CRC Press; 2000.

49.	Lyne WH. Unsteady viscous flow in a curved pipe. Journal of Fluid Mechanics. 1971;45:13-31.

50.	Germano M. On the effect of torsion on a helical pipe flow. Journal of Fluid Mechanics. 1982;125(1):1-8.

51.	Gallo D, Steinman DA, Bijari PB, Morbiducci U. Helical flow in carotid bifurcation as surrogate marker of exposure to disturbed shear. Journal of biomechanics. 2012;45(14):2398-404.

52.	Aristokleous N, Seimenis I, Georgiou GC, Papaharilaou Y, Brott BC, Nicolaides A, et al. Impact of Head Rotation on the Individualized Common Carotid Flow and Carotid Bifurcation Hemodynamics. IEEE Journal of Biomedical and Health Informatics. 2014;18(3):783-9.

53.	Morbiducci U, Ponzini R, Gallo D, Bignardi C, Rizzo G. Inflow boundary conditions for image-based computational hemodynamics: impact of idealized versus measured velocity profiles in the human aorta. Journal of Biomechanics. 2013;46(1):102-9.

54.	Chiastra C, Morlacchi S, Gallo D, Morbiducci U, Cárdenes R, Larrabide I, et al. Computational fluid dynamic simulations of image-based stented coronary bifurcation models. Journal of the Royal Society, Interface / the Royal Society. 2013;10(84):20130193.

55.	Ku DN, Giddens DP, Zarins CK, Glagov S. Pulsatile flow and atherosclerosis in the human carotid bifurcation. Positive correlation between plaque location and low oscillating shear stress. Arteriosclerosis (Dallas, Tex). 1985;5(3):293.

56.	Malek AM, Alper SL, Izumo S. Hemodynamic shear stress and its role in atherosclerosis. JAMA : the journal of the American Medical Association. 1999;282(21):2035-42.

57.	Chatzizisis YS, Coskun AU, Jonas M, Edelman ER, Feldman CL, Stone PH. Role of endothelial shear stress in the natural history of coronary atherosclerosis and vascular remodeling - Molecular, cellular, and vascular behavior. Journal of the American College of Cardiology. 2007;49(25):2379-93.

21

58.   Caro CG. Discovery of the role of wall shear in atherosclerosis. Arteriosclerosis, Thrombosis, and Vascular Biology. 2009;29(2):158-61.

59.   Himburg HA, Grzybowski DM, Hazel AL, LaMack JA, Li X-M, Friedman MH. Spatial comparison between wall shear stress measures and porcine arterial endothelial permeability. American Journal of Physiology - Heart and Circulatory Physiology. 2004;286(5):H1916-22.

60.   Hoi Y, Zhou Y-Q, Zhang X, Henkelman RM, Steinman DA. Correlation between local hemodynamics and lesion distribution in a novel aortic regurgitation murine model of atherosclerosis. Annals of biomedical engineering. 2011;39(5):1414-22.

61.   Lee S-W, Antiga L, Spence JD, Steinman DA. Geometry of the carotid bifurcation predicts its exposure to disturbed flow. Stroke; a journal of cerebral circulation. 2008;39(8):2341-7.

62.   Lee S-W, Antiga L, Steinman DA. Correlations among indicators of disturbed flow at the normal carotid bifurcation. Journal of Biomechanical Engineering. 2009;131(6):061013-7.

63.   Dean WR. LXXII. The stream-line motion of fluid in a curved pipe (Second paper). Philosophical Magazine Series 7. 1928;5(30):673-95.

64.   Prosi M, Perktold K, Ding Z, Friedman MH. Influence of curvature dynamics on pulsatile coronary artery flow in a realistic bifurcation model. Journal of Biomechanics. 2004;37(11):1767-75.

65.   Malvè M, Gharib AM, Yazdani SK, Finet G, Martínez MA, Pettigrew R, et al. Tortuosity of Coronary Bifurcation as a Potential Local Risk Factor for Atherosclerosis: CFD Steady State Study Based on In Vivo Dynamic CT Measurements. Annals of biomedical engineering. 2015;43(1):82-93.

22

1 **Table captions**

2

3 Table 1. Values of geometric descriptors for three idealized cases (T-5, T-6, T-7):

4 distance metric (DM), total torsion (TT), total curvature (TC), vessel length, average

5 radius (R_{ave}), and average tapering coefficient (T_{ave}).

6

7 Table 2. Values of geometric descriptors for the 23 vessel segments obtained from the

8 three patient-specific cases (patient-A, patient-B, patient-C): distance metric (DM), total

9 torsion (TT), total curvature (TC), vessel length, average radius (R_{ave}), and average

10 tapering coefficient (T_{ave}). Bold denotes maximum value for each patient.

11

23

Figure captions

Figure 1. Geometries for the idealized and patient-specific studies. Geometries for the idealized study: vessel models with (a) 5, (b) 6, and (c) 7 curved arcs. Geometries for the patient-specific study: patient-A (d), patient-B (e), patient-C (f). A label for each branch of the patient-specific geometries is shown.

Figure 2. (a) Idealized geometry segments considered in the post-processing of the solution. (b) An example of vessel tree splitting for patient-A.

Figure 3. Idealized cases: (a) Dimensionless pressure drop, (b) Helicity intensity h2, (c) Threshold of TAWSS for which 10% percent of the area has lower TAWSS, (d) Threshold of RRT for which 10% percent of the area has higher RRT.

Figure 4. Correlations between tortuosity metrics: (a) Total Curvature (TC) versus Total Torsion (TT), (b) Distance Metric (DM) versus TT, (c) DM versus TC. Red circles indicate data for branches LCX123-patient-A, SPT3-patient-B, and LAD24-patient-C. Black dotted line represents linear regression fit.

Figure 5. LCX123 branch of patient-A at time t = 0.558 s: (a) vessel tree geometry; (b) flow rate at the inlet; the red dot indicates the flow rate at t = 0.558 s; (c) position of three cross-sections; (d-f) axial velocity magnitude for three cross-sections; (g) wall shear stress distribution on LCX123; (h) iso-surface of LNH = ±0.4.

1 Figure 6. SPT3 branch of patient-B at time t = 0.558 s: (a) vessel tree geometry; (b)

2 flow rate at the inlet; the red dot indicates the flow rate at t = 0.558 s; (c) position of

3 three cross-sections; (d-f) axial velocity for three cross-sections; (g) wall shear stress

4 distribution on SPT3; (h) iso-surface of LNH = ±0.4.

5 Figure 7. LAD24 branch of patient-C at the time t = 0.558 s: (a) vessel tree geometry;

6 (b) flow rate at the inlet; the red dot indicates the flow rate at t = 0.558 s; (c) position of

7 three cross-sections; (d-f) axial velocity for three cross-sections; (g) wall shear stress

8 distribution on LAD24; (h) iso-surface of LNH = ±0.4.

9 Figure 8. Scatter plots showing the helicity intensity h2 calculated for each of 23 vessel

10 segments versus the tortuosity metrics DM (a), TT (b), and TC (c). The dotted line

11 shows the x-log regression fit, and R^2 is the determination coefficient.

12 Fligure 9. For each of the 23 vessel segments across all patients: (a) dimensionless

13 pressure drop per unit length (b) TAWSS90 (c) RRT90 versus corresponding

14 dimensionless helicity intensity h2. The dotted lines show the log-log regression fit. R^2 is

15 the determination coefficient.

16

25

1 **Tables**

2 Table 1. Values of geometric descriptors for three idealized cases (T-5, T-6, T-7):

3 distance metric (DM), total torsion (TT), total curvature (TC), vessel length, average

4 radius (Rave) and average tapering coefficient (Tave).

	Length (mm)	Rave (mm)	Tave (arb. units)	DM (arb. units)	TT (arb. units)	TC (arb. units)
T-5	127.9229	1.125	0.5	1.279	0	17.055
T-6	131.1199	1.125	0.5	1.311	0	20.043
T-7	134.9229	1.125	0.5	1.349	0	22.844

5

6

1　Table 2. Values of geometric descriptors for the 23 vessel segments obtained from
2　three patient-specific cases (patient-A, patient-B, patient-C): distance metric (DM), total
3　torsion (TT), total curvature (TC), vessel length, average radius (R_{ave}), and average
4　tapering coefficient (T_{ave}). Bold denotes maximum value for each patient.

|		Length (mm)	R_{ave} (mm)	T_{ave} (-)	DM (-)	TT (-)	TC (-)
Patient-A	LMCA	7.881	2.540	1.006	1.009	4.778	0.714
	LAD	42.764	1.798	1.000	1.054	12.071	1.717
	LAD24	41.502	1.192	0.970	1.114	15.262	4.592
	LCX	25.683	1.920	0.590	1.053	6.159	1.523
	LCX123	84.027	1.429	1.005	**1.344**	**26.841**	**5.297**
	MARG1	37.648	1.152	0.456	1.059	9.530	3.274
	SPT2	33.394	1.148	0.400	1.041	8.497	2.257
Patient-B	LAD	33.465	1.557	1.001	1.031	7.169	1.723
	LAD2_2	16.402	1.085	0.490	**1.200**	6.133	2.495
	LCX	13.651	1.607	0.411	1.010	5.754	0.970
	LCX1	36.428	1.362	0.999	1.070	11.515	2.253
	ATR	18.994	0.917	0.514	1.133	5.327	2.296
	MARG2	18.742	1.170	0.508	1.173	8.520	5.368
	SPT2	18.626	1.128	0.527	1.030	8.163	1.177
	SPT3	30.647	1.022	0.858	1.123	**14.275**	**6.526**
Patient-C	LAD_1	17.574	1.998	0.998	1.045	5.831	1.366
	LAD_2	20.874	2.062	1.006	1.015	9.463	0.885
	LAD1	26.893	1.564	1.006	1.170	7.078	3.383
	LAD24	43.672	1.295	1.006	**1.228**	**16.677**	**5.732**
	LCX	18.675	1.933	0.411	1.014	8.117	0.805
	LCX12	54.162	1.238	1.003	1.109	9.175	2.186
	MARG1	63.429	1.696	1.004	1.180	13.520	3.472
	SPT2	34.560	1.523	0.540	1.043	9.435	1.717

5

6

7

27

1 **Figures**

2

3
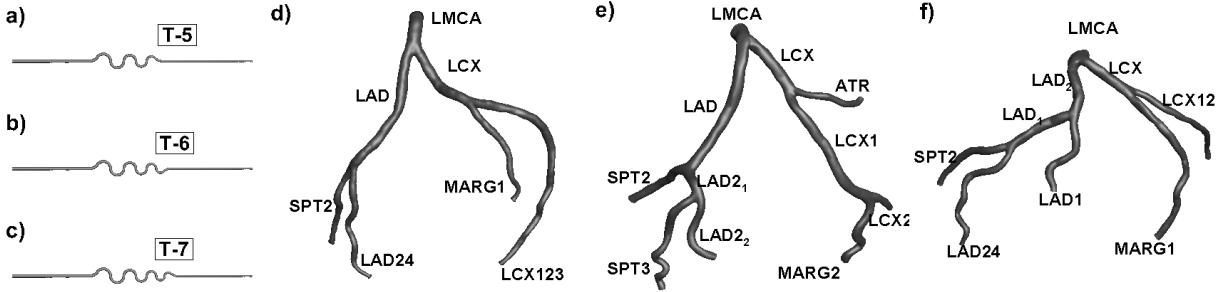
4 Figure 1. Geometries for the idealized and patient-specific studies. Geometries for the

5 idealized study: vessel models with (a) 5, (b) 6, and (c) 7 curved arcs. Geometries for

6 the patient-specific study: patient-A (d), patient-B (e), patient-C (f). A label for each

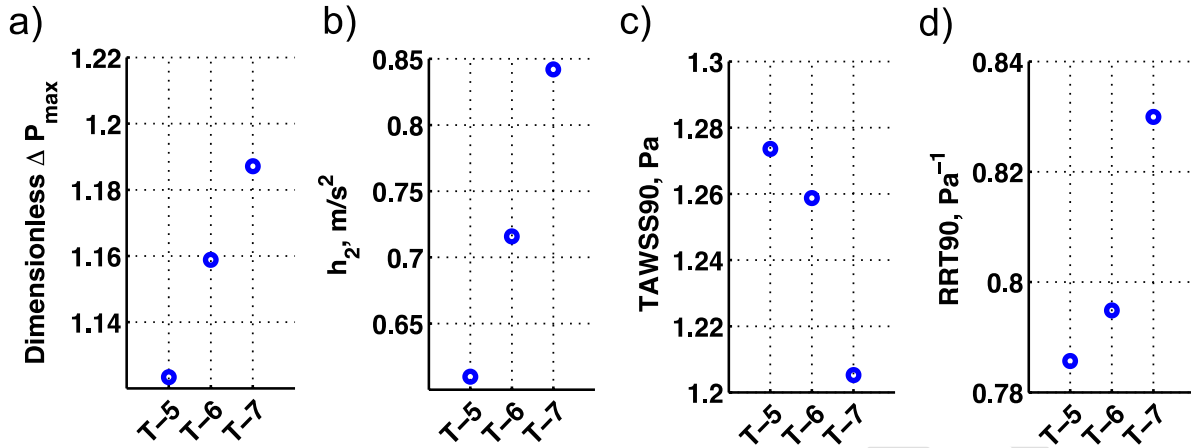7 branch of the patient-specific geometries is shown.

8
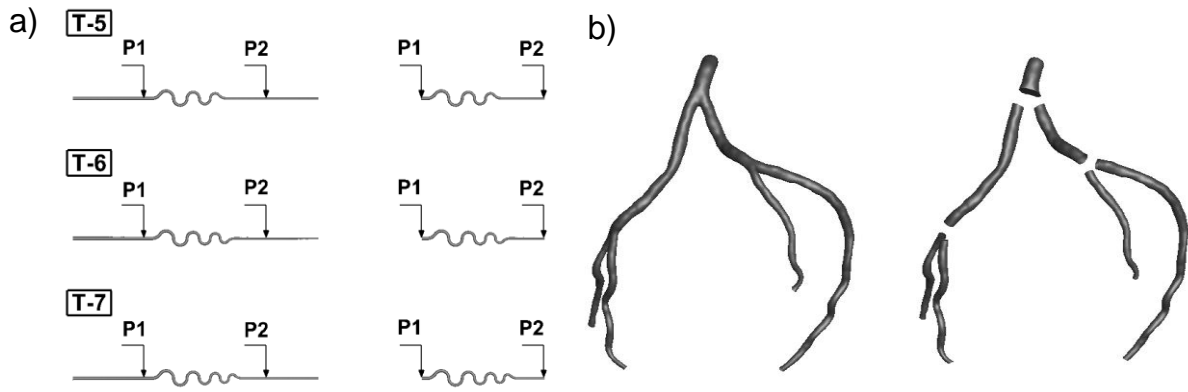
1

2 Figure 2. (a) Idealized geometry segments considered in the post-processing of the
3 solution. (b) An example of vessel tree splitting for patient-A.

4

Figure 3. Idealized cases: (a) Maximum dimensionless pressure drop per unit length, (b) Helicity intensity h_2, (c) Threshold of TAWSS for which 10% percent of the area has lower TAWSS, (d) Threshold of RRT for which 10% percent of the area has higher RRT.
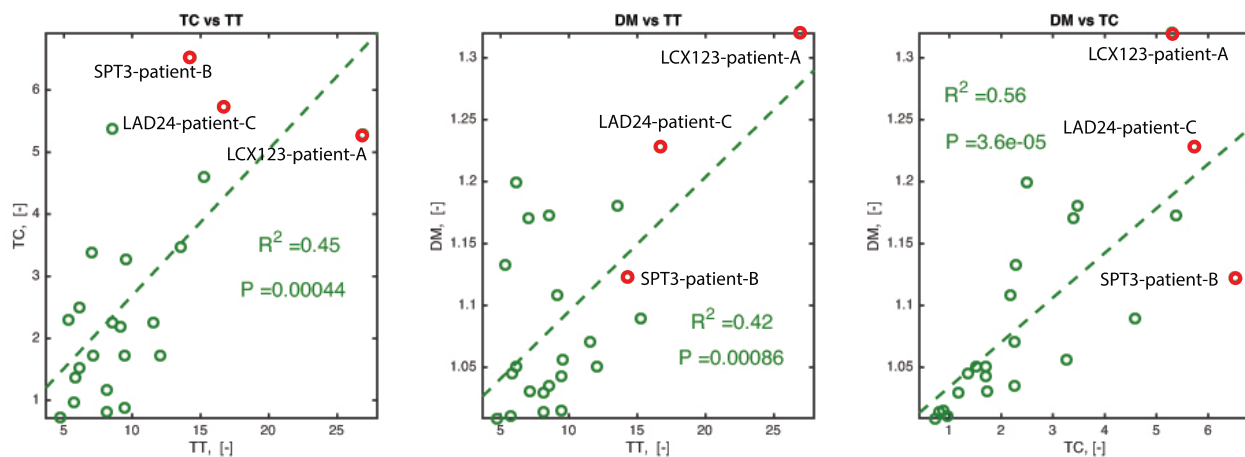
1

2 Figure 4. Correlations between tortuosity metrics: (a) Total Curvature (TC) versus Total
3 Torsion (TT), (b) Distance Metric (DM) versus TT, (c) DM versus TC. Red circles
4 indicate data for branches LCX123-patient-A, SPT3-patient-B, and LAD24-patient-C.
5 Black dotted line represents linear regression fit. R^2 is the determination coefficient, P is
6 the p-value.

7
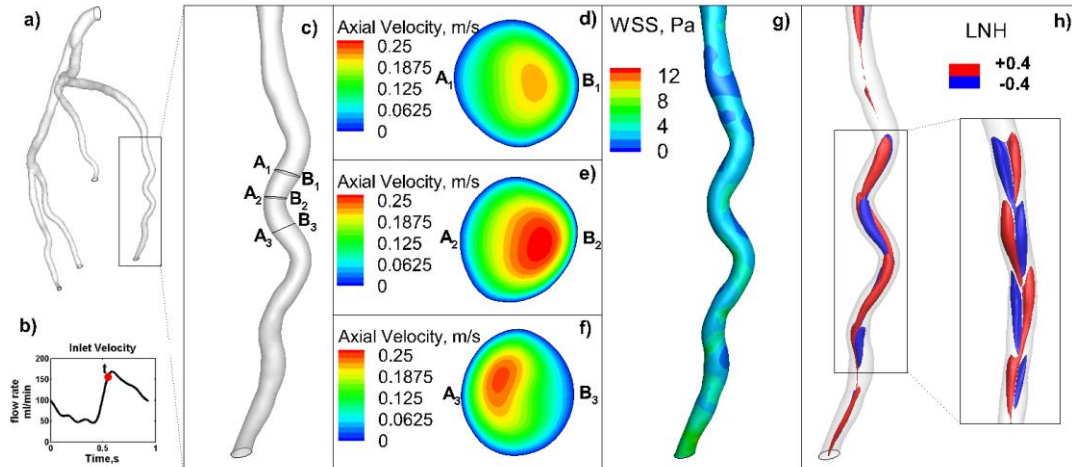
Figure 5. Geometry and flow characteristics for the LCX123 branch of patient-A at time t = 0.558 s: (a) vessel tree geometry; (b) flow rate at the inlet of the branch, with the red dot indicating the flow rate at t = 0.558 s; (c) position of the three selected cross-sections; (d-f) axial velocity magnitude at these three cross-sections; (g) WSS distribution; and (h) iso-surfaces of LNH = ±0.4.
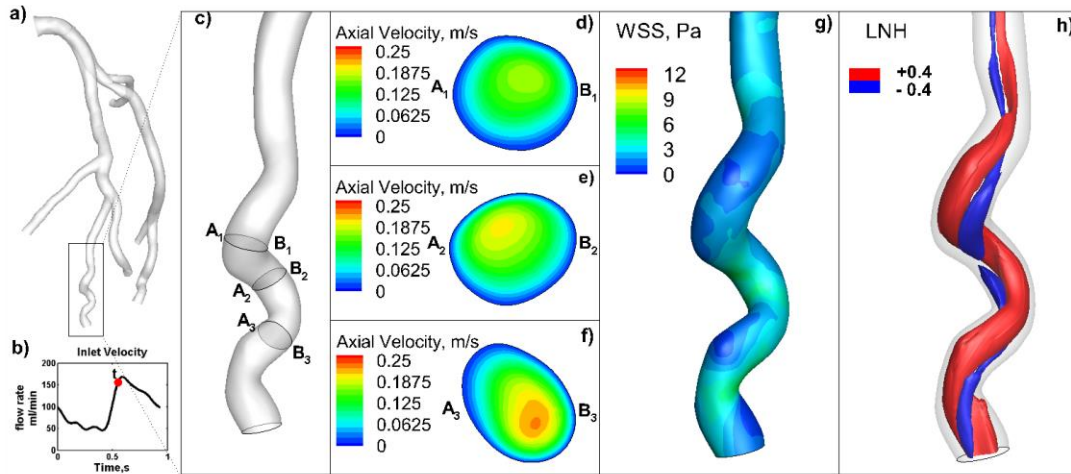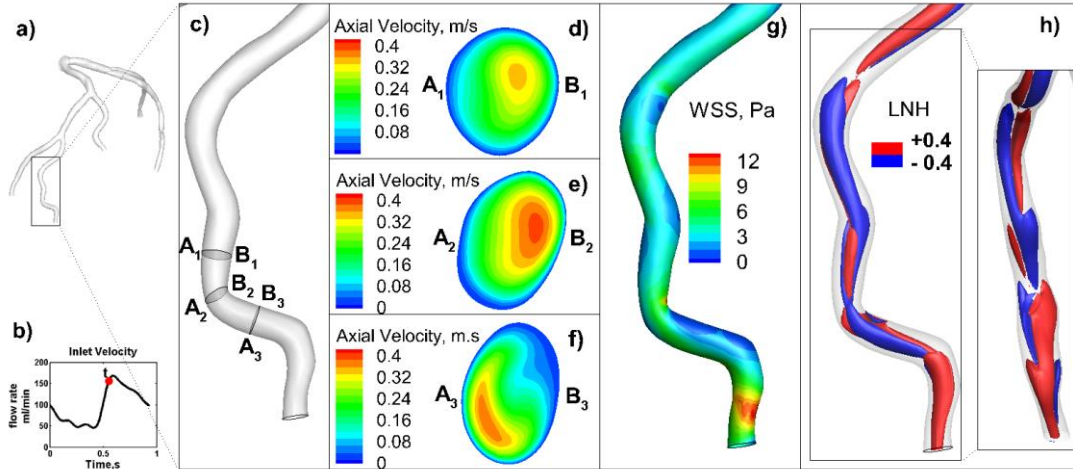
32

Figure 6. Geometry and flow characteristics for the SPT3 branch of patient-B at time t = 0.558 s: (a) vessel tree geometry; (b) flow rate at the inlet of the branch, with the red dot indicating the flow rate at t = 0.558 s; (c) position of the three selected cross-sections; (d-f) axial velocity at these three cross-sections; (g) WSS distribution; and (h) iso-surfaces of LNH = ±0.4.
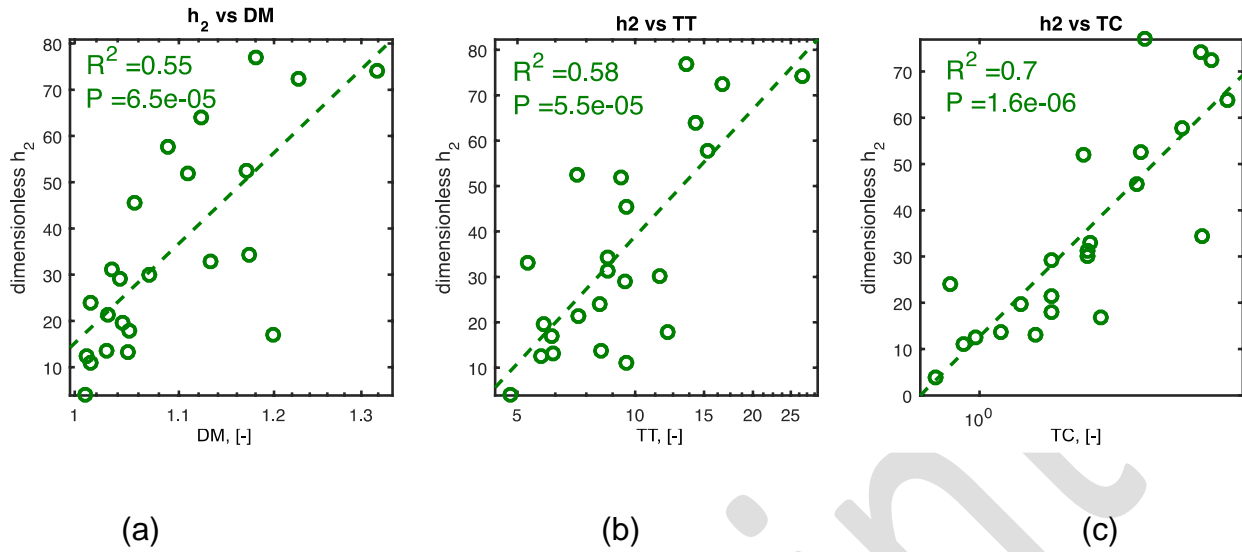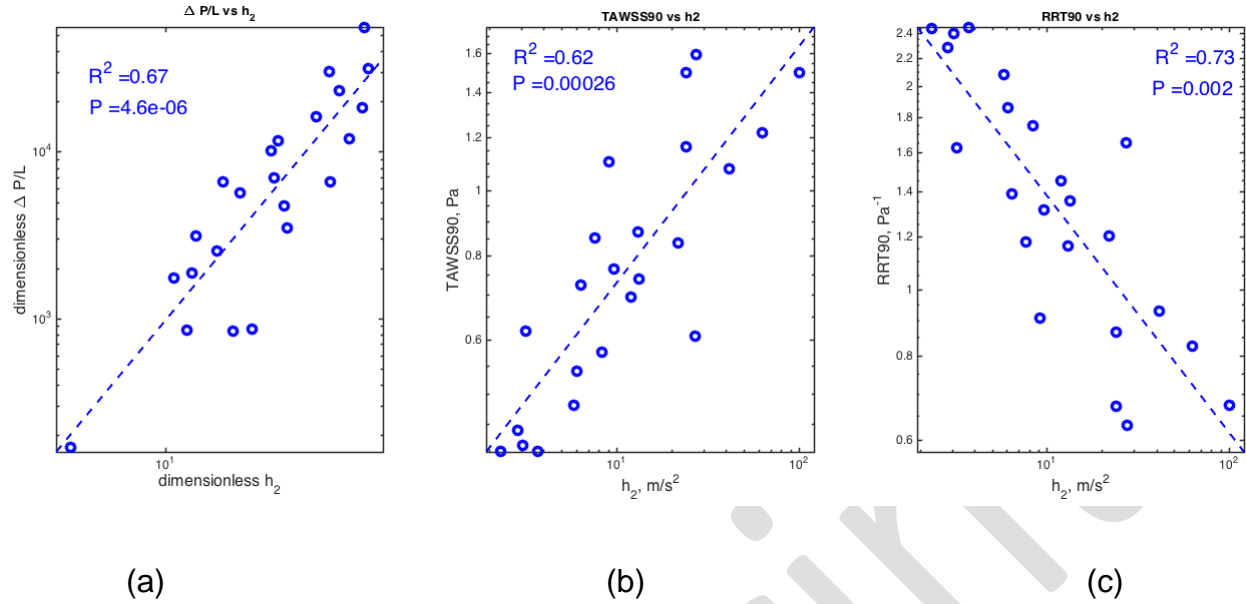
33

Figure 7. Geometry and flow characteristics for the LAD24 branch of patient-C at time t = 0.558 s: (a) vessel tree geometry; (b) flow rate at the inlet of the branch, with the red dot indicating the flow rate at t = 0.558 s; (c) position of the three selected cross-sections; (d-f) axial velocity at these three cross-sections; (g) WSS distribution; and (h) iso-surfaces of LNH = ±0.4.

34

Figure 8. Scatter plots showing the dimensionless helicity intensity h_2 calculated for each of 23 vessel segments relative to the tortuosity metrics DM (a), TT (b), and TC (c). The dotted line shows the x-log regression fit; R^2 is the determination coefficient, P is the p-value.

Figure 9. Comparison of flow characteristics with the (dimensionless) helicity intensity for each of the 23 vessel segments across all patients: (a) dimensionless pressure drop per unit length, (b) TAWSS90, and (c) RRT90. The dotted lines show the log-log regression fit; R^2 is the determination coefficient, P is the p-value.

36